CHAPTER 2

Material synthesis and methods of characterization

2 Material synthesis and methods of characterization

In this chapter, the materials synthesis process is discussed in details. A brief discussion of each of the experimental characterization and computational techniques adopted is given here.

2.1 Details of characterization techniques adopted

The present work reports the synthesis of nanomaterials using solid state reactions followed by ultrasonication as described in section 2.2 here. The XRD analysis of the as-synthesized powdered samples were performed using X-ray Diffractometer (make: RIGAKU MINIFLEX) with Cu-Kα radiation (λ= 1.5405 Å) in the 2θ range from 10º to 70º. EDX spectra of the samples were obtained using INCAx-sight EDS detector and electron micrographs were obtained using an SEM (make: JEOL JSM-6390LV). For the study of the optical BG and photocatalytic activity in the UV-vis band, spectral analysis of all as-prepared samples were done using UV-vis absorption spectrometer (make: UV 2450, SHIMADZU CORPORATION). The photocatalytic activity of the prepared samples was studied under the influence of light emitted from a Xenon arc lamp (Xenon Lamp Zolix SLH- X500 Xenon Arc Light Source which provides UV to visible light) having output power of 500W (output intensity 12000lux measured at 8cm from the light source). Electron micrographs were also obtained using a TEM (make: TECNAI G2 20 S-TWIN, 200KV, FEI USA) so as to obtain the structural information. The concept of Berrett-Joyner-Halenda (BJH) pore size distribution and Brunauer-Emmett-Teller (BET) theory were employed to determine the surface area of the materials by analyzing N_2 adsorption/desorption isotherm using a NOVA 1000E BET instrument (QUANTA CHROME). Raman spectra were obtained using Lab Ram HR Laser Micro Raman System and PL study was performed with a F-2700 FL Spectrophotometer.

2.2 Experimental details of material synthesis process

In this section, the material synthesis process is reported. Different synthesis processes like mechanical exfoliation using the scotch-tape micromechanical cleavage technique, exfoliation by lithium intercalation followed by ultrasonication, solid state reaction

mechanism, hydrothermal techniques, CVD, ALD etc. have been reported for synthesizing monolayer to few layers of TMDs [1-8]. In our work, the solid state reaction mechanism for the synthesis of MoS_2, WS_2 and ternary compound MoW-disulfide NPs was adopted and the chemical equations involved are given in equations (2.1-2.3)[3,4]. Solid state reaction is a solvent-free reaction in which all the raw materials used are in solid form. In our material synthesis process the raw chemicals i.e molybdic acid, tungstic acid and thiourea were all in powdered form.

$$H_2MoO_4 + 48NH_2CSNH_2 \xrightarrow[N_2]{500°C} \text{few layers of } MoS_2 \quad (2.1)$$

$$H_2WO_4 + 48NH_2CSNH_2 \xrightarrow[N_2]{500°C} \text{few layers of } WS_2 \quad (2.2)$$

$$H_2MoO_4 + H_2WO_4 + 48NH_2CSNH_2 \xrightarrow[N_2]{500°C} MoW-\text{disulfide compound} \quad (2.3)$$

For the material synthesis purpose, commercially available Molybdic acid (RANKEM (M0240)), Tungstic acid (Himedia (RM6308-100G)), and Thiourea (RANKEM (T0050)) were chosen as the raw materials. The chemicals were at first separately ground mildly using a mortar and pestle to make a fine powder of each chemical and were weighed separately using a chemical balance (make: Denver Instrument). These were then mixed in the proper molar ratio in a silica combustible boat and the boat was kept inside the furnace. The furnace was then set at 500ºC for 3hours with a continuous supply of N_2. After 3hours of continuous heating, the product was left to cool in the N_2 environment for another 4/5hr till the furnace cooled to room temperature. The blackish products (flakes) were next collected for purification and further investigation. A schematic of the set-up used for this synthesis is shown in figure 2.1(a). A photograph of the experimental set-up for material synthesis is shown in figure 2.1(b).

For the synthesis of MoW-disulfide compound, molybdic acid and tungstic acid with excess thiourea as the raw materials were taken and their percentage compositions were estimated using SEM-EDX spot analysis. Molybdic acid and tungstic acid were mixed in the molar ratio 1:1 and 10:1 and the respective compounds were named as MoW-disulfide1 and MoW-disulfide2.

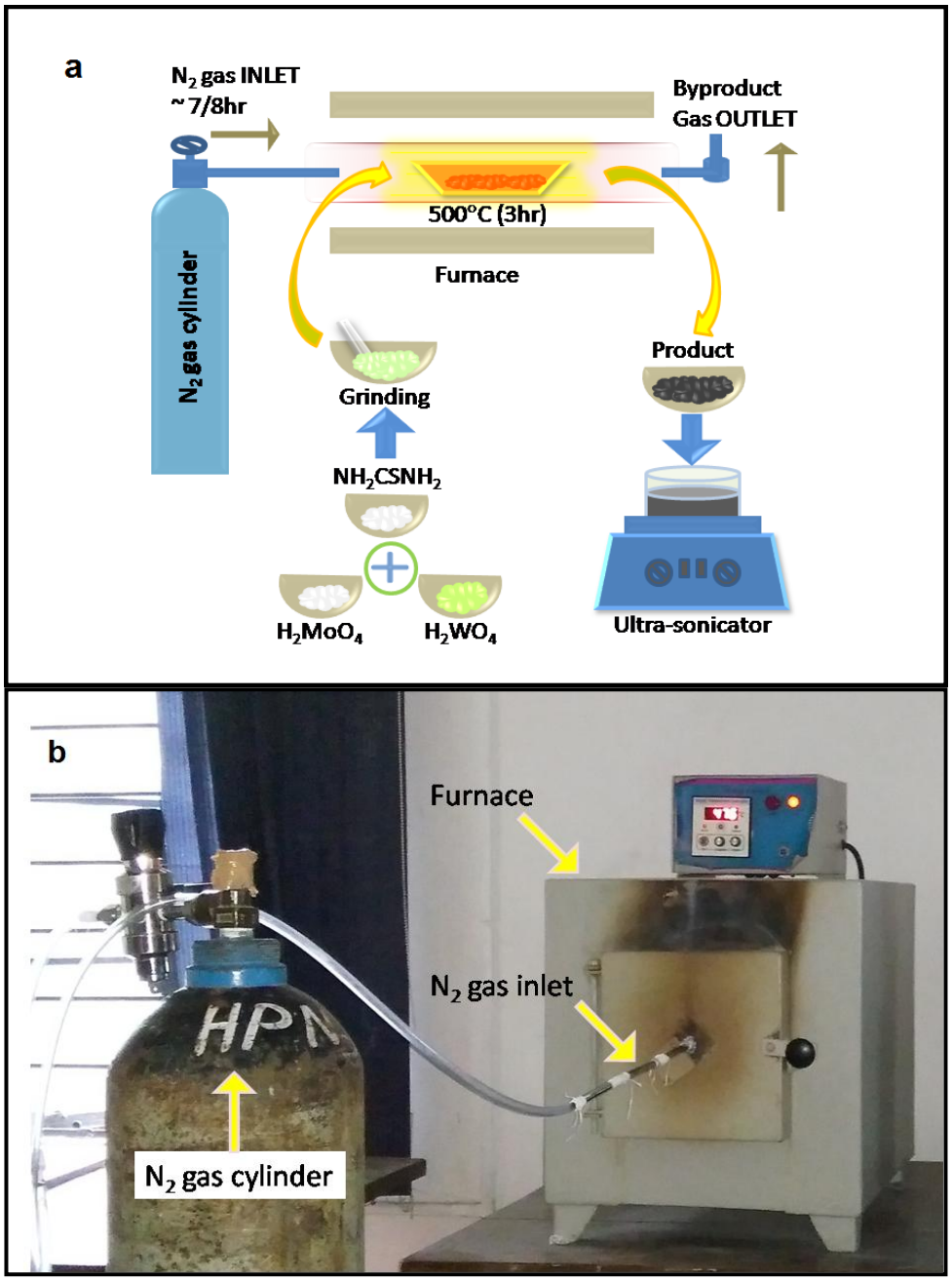

Figure 2.1 (a) Schematic of the experimental set-up for material synthesis. In the synthesis process, the powdered raw materials are mixed thoroughly and heated at 500°C for 3hours followed by cooling to room temperature under N_2 gas environment inside a furnace to produce the final product and (b) a photograph of the experimental set-up for material synthesis.

In order to ascertain that the as-prepared MoS_2, WS_2 and compound MoW-disulfide samples did not contain oxides and other similar water-soluble impurities, the samples were cleaned initially with ethanol. Thereafter, these were cleaned with warm distilled water at 70°C for one hour to remove the water-soluble contents and were centrifuged for 12min at 6000rpm. The colored water content was pipetted out and the residual sample sedimented at the bottom. This cleaning process was repeated until the water became clear. The final water content was removed by pipette. After removing the water-soluble content the samples were dried at 70°C for approximately 12hours. The dry product was then ground uniformly using mortar and pestle to make a fine powder. This powder was mixed with distilled water and stirred in a magnetic stirrer. In order to prepare nano-sized particles, the samples were dispersed in distilled water and ultrasonicated for several hours so that the larger particles broke into nanoscale-sized smaller particles.

There are reports which affirm that at high temperature, above 300°C, if, somehow, transition metal trisulfide compound is formed they readily get decomposed into disulfide compound and sulfur [9-11]. Since, in our work, the synthesis temperature is 500°C, there is no possibility of forming MoS_3, WS_3 or trisulfide ternary compounds. Also, the polycrystalline nature of our as-prepared materials reaffirms the formation of TMD compounds since trichalcogenides are reported to be amorphous materials [12].

2.3 X-ray diffraction technique

X-ray diffractometer is an analytical technique for the study of crystal structure which provides information on lattice dimension. Max von Lau, in 1912, discovered that crystalline substances act as a three-dimensional diffraction grating, the spacings of which are comparable with X-ray wavelengths [13]. When monochromatic X-ray is incident on any crystal, diffraction occurs. The maxima of diffraction satisfy the Bragg's law

$$2d_{hkl}\sin\theta = m\lambda \qquad (2.4)$$

where λ is the wavelength of incident X-ray, m is the order of diffraction, d_{hkl} is the crystal plane spacing and θ is the Bragg's angle [14]. The diffraction pattern allows us to determine the spacing of crystal planes which provides identification of the material under investigation using appropriate software.

In our work, XRD studies were carried out using a Rigaku Miniflex diffractometer.

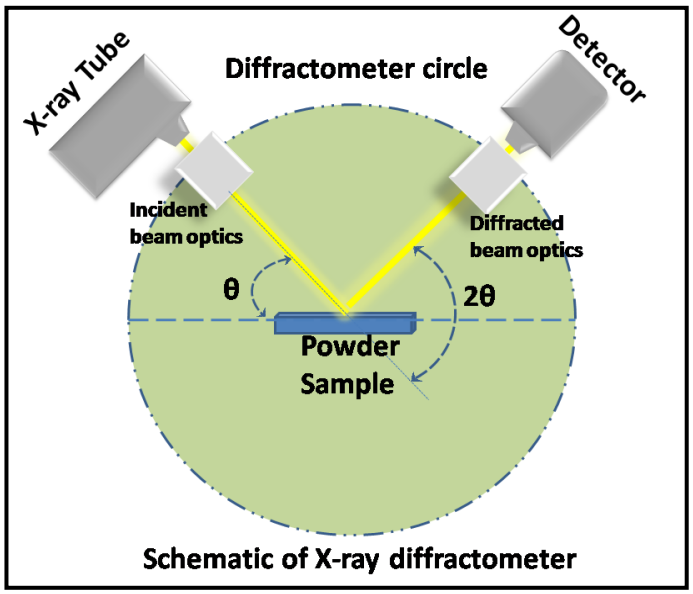

Figure 2.2 Schematic diagram of the X-ray diffractometer technique for the analysis of powder sample.

The materials to be analyzed were finely ground and homogenized. This powder sample was subjected to XRD analysis.

Inside the diffractometer, the rays are generated by a cathode ray tube in which high energy electron beam strikes a copper anode to produce Cu-kα radiation having wavelength λ=1.5405Å. The X-rays are then filtered to obtain monochromatic rays which are collimated and directed towards the specimen sample. The diffracted rays are collected by a charge coupled device (CCD) detector. The detector produces pulses proportional to the intensity of diffracted rays. Thus an intensity versus diffraction angle plot is obtained using the monitored data. During data collection, a goniometer rotates the sample holder step by step in the 2θ range from 10º to 70º while the sample is exposed to radiation. In our work, the step size was maintained at 0.5º. From the intensity versus 2θ plot the Bragg's angles corresponding to maxima can be obtained which in turn correspond to interplanar spacing that can be calculated using Bragg's equation. These values are then compared with the standard data available in the joint committee on powder diffraction standards (JCPDS) software to identify the required specimen. The schematic diagram of X-ray diffractometer operation is shown in figure 2.2.

2.4 Transmission electron microscopy

TEM produces high-resolution 2D images which provide crystallographic, morphologic and compositional information of the specimen samples [15]. The resolution of TEM image is so high that (For an electron with K.E. = 1eV and rest mass energy 0.511MeV, the associated De Broglie wavelength is 1.23 nm, about a thousand times smaller than a 1eV photon whose De Broglie wavelength is 1240nm) it allows us to view a sample on a molecular level. The basic principle of TEM is similar to that of an optical microscope; the only difference is TEM uses an electron beam to produce images instead of light as in an optical microscope. Owing to the smaller de Broglie wavelength of electrons TEM produces a resolution thousand times better than of an optical microscope. Inside the TEM, the electron source emits high voltage energetic electron beam that travels through vacuum and is focused and collimated by an electromagnetic lens system. The beam then interacts with the specimen which is most often an ultrathin section few nm thick or a suspension on a grid. Depending on the density of the specimen part of the electron beam get scattered

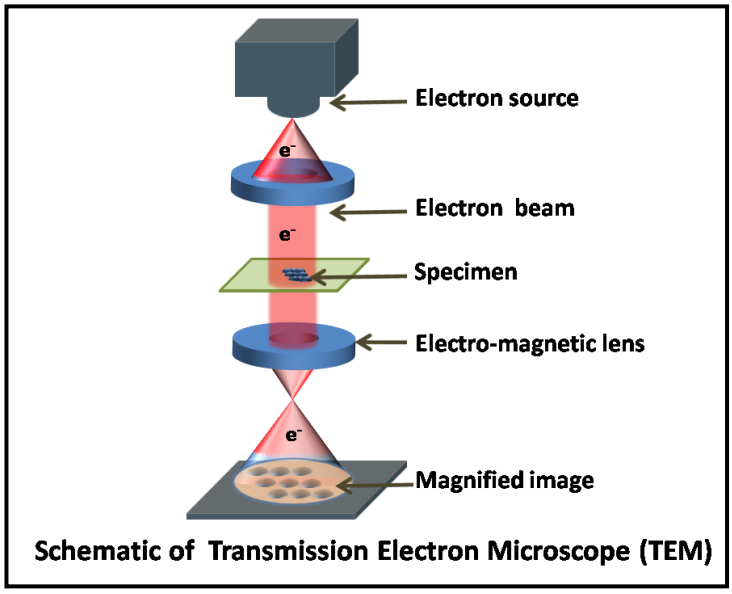

Figure 2.3 Visualization of TEM technique producing a magnified image of the specimen.

and partly gets transmitted forming a shadow image of the specimen. The brighter areas of the image represent places of lower density of the sample where a greater number of electrons are able to pass and the darker areas reflect the dense areas of the sample and thus provide information of size, structure, shape and texture of the specimen. A schematic of the TEM producing a magnified image of the specimen is shown in figure 2.3.

2.5 Scanning electron microscopy and energy dispersive X-ray spectroscopy

An SEM is a type of electron microscope which produces a high-resolution image of the sample surface [15]. The SEM images help us to view the surface morphology of the sample and provide topographical information such as layer thickness and other quantitative information. An SEM consists of an electron source, electromagnetic (e.m.) lenses and an electron detector (Figure 2.4). It uses an electron beam instead of light to provide a high-resolution image. An electron gun emits electrons, the amount of which is controlled by the condenser lens. The electron beam is accelerated and focused on the specimen by using an e.m. lens system. A deflection coil helps to deflect the focused beam for scanning the sample surface. The sample emits secondary electrons, which are then detected by a secondary electron detector. The number of detected electrons is a function of surface morphology. By scanning the beam and detecting the variation of the number of emitted electrons, one can reconstitute the surface topography.

This electron microscope also provides information of elementary composition of the sample by obtaining EDX spectra. The electron beam also excites the atoms of the sample and ionize them thereby generating secondary X-rays. The energy of these X-rays depends on the elementary composition of the sample. By identifying these characteristic X-rays and detecting their energy using appropriate software, one can reveal the composition and measure the abundance of elements present in the sample so as to deduce the chemical nature of the material and its spatial variation. Other types of interactions between the beam and the surface allow various complementary analyses to be done. SEM thus helps to obtain a magnified image of the surface of thick samples and analyze their composition.

Using EDS, the abundance of specific elements and chemical composition of a material can be envisioned from elemental maps or spot chemical analysis. EDX can analyze a

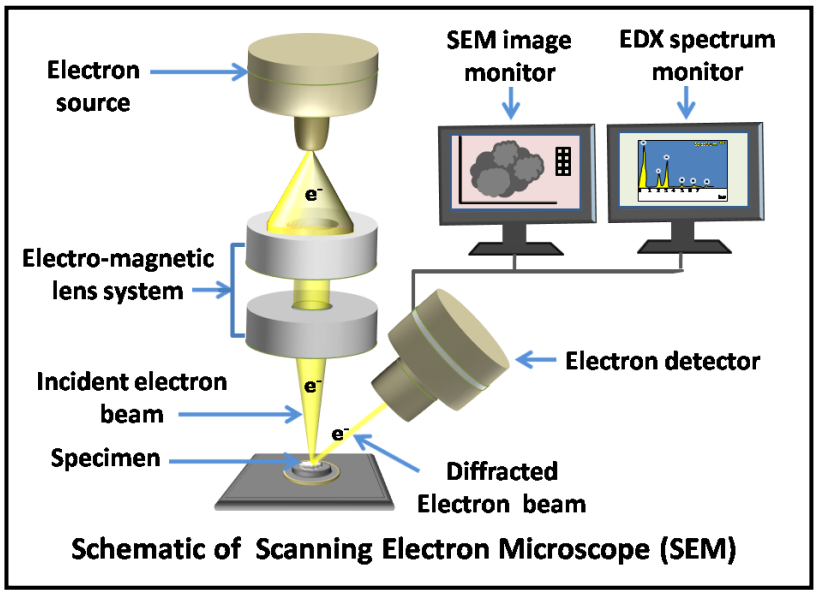

Figure 2.4 SEM used to obtain a magnified image and EDX spectrum.

single spot to give a spectrum that provides information about the elemental composition. An elemental map of SEM is a series of EDX analyses spread across a pre-defined area of the sample. It represents the intensities of the peaks from each element at each point in a particular color in a map showing where that element is most abundant. Several elements can be simultaneously detected to produce maps of the distribution of each element across the same area.

2.6 Raman spectroscopy

Raman spectroscopy deals in inelastic scattering of monochromatic light when it interacts with matter [16]. This spectroscopic technique is used to observe rotational, vibrational and other low-frequency modes that exist in a material system which forms a structural fingerprint of the system. The primary components of a Raman spectrometer are a laser light source used as an excitation source, a microscope or a fiber optic probe as sampling apparatus and a spectrometer having a CCD as a detector as shown in figure 2.5.

In Raman spectroscopy, a laser light in the visible, near infrared (IR) or near UV range is used to probe the material. The light interacts with the molecular vibrations, phonons or other electronic transition states of the material resulting in a change in polarizability of the electrons in the molecules and scattering of the probing light photons. This results in a shift in the energy of the scattered photons. If the frequency of the incident photon is ν_0 the frequency of the scattered photon is shifted to $\nu_0 \pm \Delta\nu$. The scattered photon that is shifted to frequency $\nu_0-\Delta\nu$ is called stokes light and to frequency, $\nu_0+\Delta\nu$ is called anti-Stokes light. The anti-Stokes light is much weaker than Stokes light. The shift in frequency provides characteristic information of spatial orientation of the material. A filter is used to collect the Raman scattered Stokes light and filters out the Rayleigh and anti-Stokes light. A diffraction grating disperses the Raman shifted light according to wavelength and a highly sensitive CCD detector detects the signal which is then fed to a computer for decoding. Energy level diagram showing transition in Raman spectroscopy is given in figure 2.6.

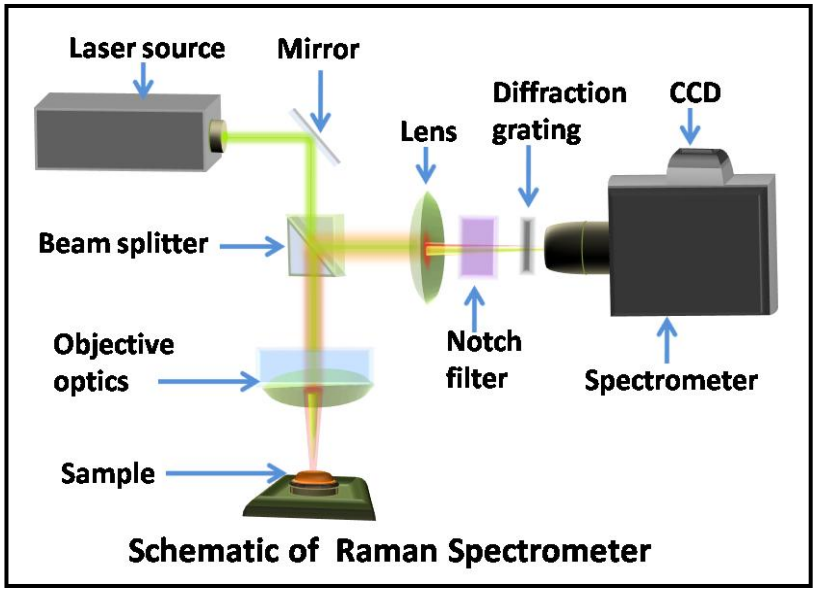

Figure 2.5 Schematic diagram showing the mechanism of Raman spectrometer.

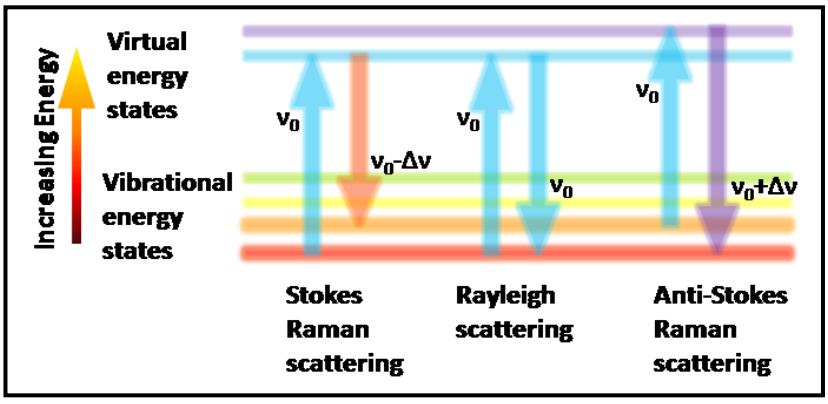

Figure 2.6 Energy level diagram showing transitions in Raman spectra.

2.7 UV-Visible spectroscopy

A UV-vis spectrometer consists of a light source which emits light in UV to visible range, a monochromator, sample and reference cells, a detector and a recording device. In figure 2.7, a schematic diagram of the UV-vis spectrometer is shown to visualize the working of the spectrometer. The monochromator consists of a light dispersion device, usually a rotating prism and a slit. The various wavelengths separated by the prism are selected by the slit such that the rotation of the prism results in continuously increasing wavelengths to pass through the reference cell and the sample cell with the help of a beam splitter. The cells are made of some kind of transparent material like quartz which does not absorb light. Finally, the emerging and scattered lights are detected by detectors. The signals are then amplified and fed into a recording device.

UV-vis spectroscopy is a type of absorption spectroscopy used in analytic chemistry for quantitative determination of analytes which may be solids, liquids or even gases. The basic principle of UV-vis spectrometer relies on Beer-Lambert law [17]. The Beer-Lambert law defines the relation between absorbance and transmittance of light through a medium (Figure 2.8). The law is expressed as

$$\text{Absorbance, } A = \log_{10}\frac{I_0}{I} = \log_{10}\frac{1}{T} = a(\lambda)bC \tag{2.5}$$

where A is the absorbance of light for the attenuation during propagation through an absorbing material, T is the transmittance, I_0 is the incident light intensity, I is the intensity of the transmitted light, $a(\lambda)$ is a wavelength dependent absorptivity constant, b is the length through which light propagates and C represents the analyte concentration.

In our work, since the synthesized materials are solids, therefore, we also obtain reflectance spectra which can be related to absorption spectra using Kubelka-Munk (KM) function F(R),

$$F(R) = \frac{(1-R)^2}{2R} \tag{2.6}$$

where R is the reflection coefficient [18]. We have used the KM relation to obtain the optical BGs of the as-synthesized materials. Also, the absorption spectra are obtained to study the photocatalytic behavior of the as-synthesized material.

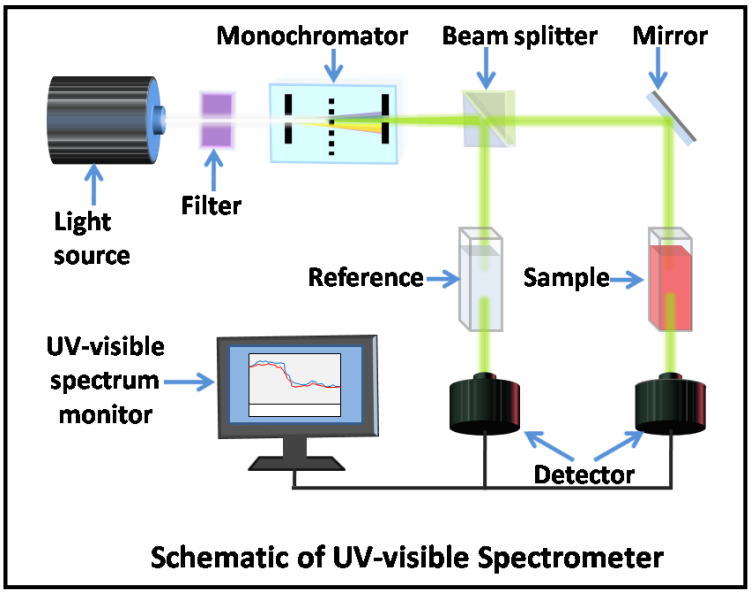

Figure 2.7 Schematic diagram of a UV-vis spectrometer showing its different components.

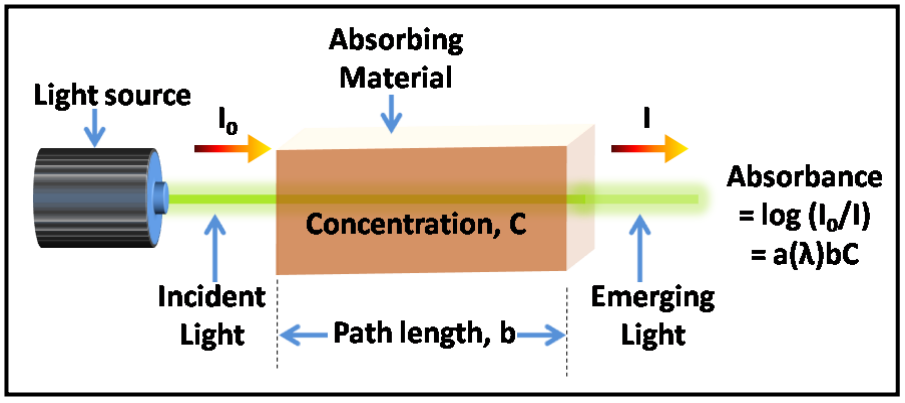

Figure 2.8 Schematic diagram to visualize Beer-Lambert Law.

2.8 Photoluminescence spectroscopy

Luminescence is the phenomenon which involves absorption of energy and subsequent emission of light by any matter [19]. When the absorbed energy is in the form of light radiation the luminescence is called PL. When light photon is absorbed by electrons they get excited to higher energy levels and then relaxes back to lower energy levels by emitting photons having different energy, usually lower energy than that of incident energy, in different time period ranging from femtosecond to millisecond or even more, such as in minutes and hours depending on the nature of the material. The intensity and spectral content of this PL is a direct measure of various important properties of the material. The schematic diagram of a PL spectrometer is shown in figure 2.9. From the light source, an excitation wavelength is selected by a first monochromator and luminescence is observed through a second monochromator. The second monochromator is usually positioned at 90° to the incident light to optimize the intensity of scattered light reaching the detector. For a particular excitation wavelength, we can record the emission spectrum by scanning the emitted radiation by the sample.

2.9 Brunauer-Emmett-Teller theory and Barrett-Joyner-Halenda concept

The true surface area of low dimensional material, including irregularities in surface and pore interiors, cannot be calculated from particle size information but is determined at the atomic level by the adsorption of an unreactive or inert gas. BET theory serves as the basis of the technique to measure such surface area and pore size distribution [20]. Among various gases, nitrogen gas is available in high purity and it has a strong interaction with most solids and hence adsorption of nitrogen gas is analyzed by BET theory. Because of the weak interaction between the gas and solid the sample surface is cooled using liquid nitrogen to obtain the detectable amount of adsorption. Nitrogen gas is released slowly over the sample at low relative pressure, lower than atmospheric pressure. No more gas is adsorbed after attaining the saturation pressure. The change in pressure is monitored using sophisticated pressure transducer with high precision and accuracy. After the formation of adsorbed gas layers, the sample is isolated and heated so that the sample releases the adsorbed nitrogen gas and thereafter it is quantified. From the collected data, plot of the

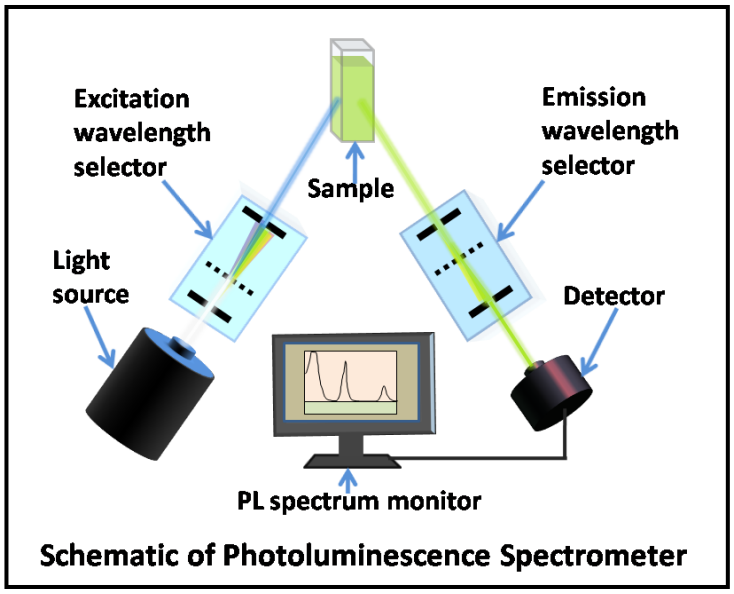

Figure 2.9 Schematic diagram of the PL spectrometer technique.

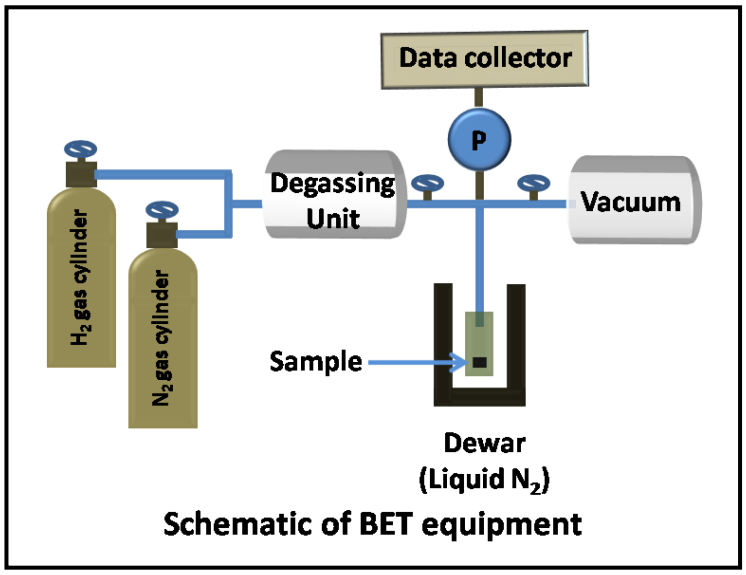

Figure 2.10 Schematic diagram of BET measurement technique.

amount of adsorbed gas vs relative pressure, known as BET isotherm, is obtained. BET theory relies on the fact that the amount of gas adsorbed on a solid depends not only on the exposed surface area but also on the temperature, gas pressure and strength of interaction between the gas and solid. This theory is an extension of the Langmuir theory of adsorption and is applicable for multilayer adsorption. The BET equation can be expressed as equation 2.7.

$$\frac{P}{v(P_0 - P)} = \frac{1}{v_m C_1} + \frac{C_1 - 1}{v_m C_1}\left(\frac{P}{P_0}\right) \tag{2.7}$$

where v is the amount of nitrogen adsorbed at a given relative pressure (P/P_0), v_m is the amount of gas adsorbed at standard temperature and pressure (STP) known as monolayer capacity, P and P_0 are the equilibrium and the saturation pressure of adsorbates at the temperature of adsorption and C_1 is a constant expressed in equation 2.8 [20, 21].

$$C_1 = \exp\left(\frac{E_1 - E_n}{RT}\right) \tag{2.8}$$

where E_1 and E_n are the heat of adsorption of the first and nth layers respectively. The quantity v_m and C_1 are calculated from the plot $P/v(P_0 - P)$ vs P/P_0. The surface area is determined by using relation 2.9 and 2.10.

$$S_{total} = \frac{v_m N_A s}{V} \tag{2.9}$$

$$S_{BET} = \frac{S_{total}}{w} \tag{2.10}$$

where N_A is Avogadro's number(equal to 6.23×10^{23}), s is the adsorption cross-section of the adsorbing species (16.2Å for N_2 gas), V is the molar volume of the adsorbate gas and w is the mass of the solid sample or adsorbent. The schematic of BET measurement is shown in figure 2.10.

BJH theory is applied for calculating pore size distributions from experimental isotherms using the Kelvin model of pore filling. Assuming cylindrical geometry the average pore radius (r_p) can be expressed as equation 2.11.

$$r_p = \frac{2V_p}{S_{BET}} \tag{2.11}$$

where V_p is the pore volume equal to the volume of liquid N_2 in pores (assuming pores are filled with liquid adsorbate). V_p is obtained using relation 2.12.

$$V_p = \frac{P\,v\,V_m}{RT} \tag{2.12}$$

where P is the ambient pressure, T is ambient temperature, V_m is the molar volume of liquid nitrogen (34.7cm^3/mol) and v is the volume of N_2 adsorbed [21].

2.10 Photocatalytic activity

Photocatalysis is a catalyst-enhanced reaction in the presence of light. The photocatalytic activity of our as-prepared samples as catalyst are investigated under the influence of light emitted from a xenon arc light source which provides white light in the range ultraviolet to visible wavelength. We have chosen MO and RB as model dyes due to their harmful effect and study their degradation through the influence of our prepared photocatalysts [18]. The degradation is evaluated by monitoring the decrease in the maximum UV-vis light absorbance of the dye solution in water using our synthesized catalyst after different times of light exposure. For this purpose, a 10µM solution of each dye was prepared. The catalyst material was then added to the solution and stirred in a magnetic stirrer for several hours in dark to attain absorption-desorption equilibrium. Then the stirred mixture was kept 8cm below the xenon source light and exposed to radiation. 10ml of the solution was taken out at definite intervals such that there was no further light exposure to this part of the solution. These solution samples were then centrifuged at 7000rpm so that the catalyst particles are separated from the dye solution. 3ml of the aliquot was taken from each sample for further analyses and study the UV-Vis absorption behavior [18]. The percentage of degradation (%D) of the absorbance peak for the catalytic reaction is determined using

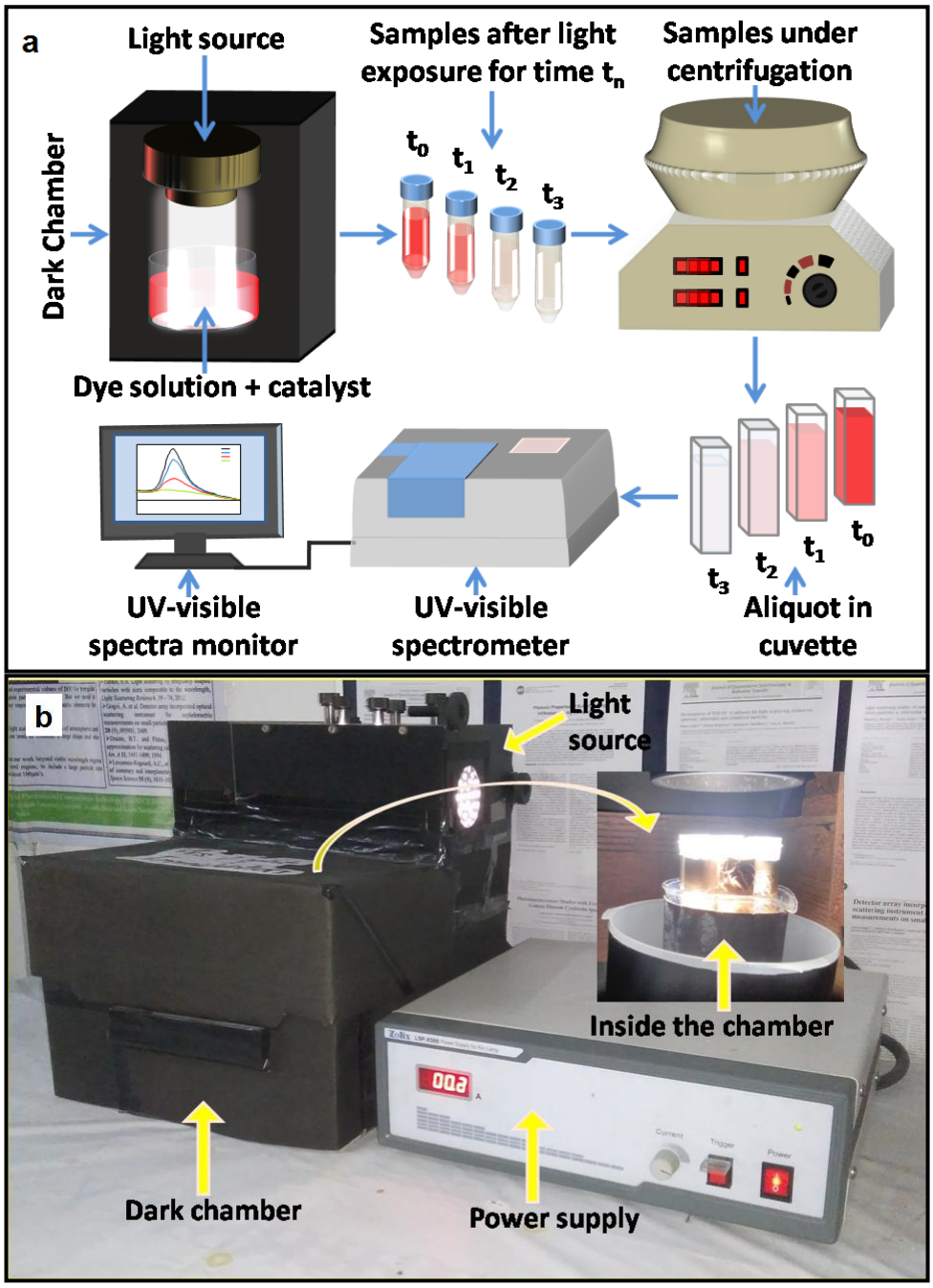

Figure 2.11 (a) Schematic diagram of photocatalytic measurement set-up and (b) a photograph of the experimental photocatalytic measurement set-up.

equation 2.13[17, 18].

$$\%D = \left\{ \frac{(A_0 - A_t)}{A_0} \right\} \times 100\% \quad (2.13)$$

where A_0 and A_t are the initial absorbance and absorbance after exposure to light for time t. We have also studied the kinetics of photocatalytic reaction using three kinds of reaction mechanism namely pseudo first order (Langmuir-Hinshelwood or L-H) mechanism, polynomial fitting and zero order mechanism which is explained in chapter 4 in details [17, 22-24]. The schematic of photocatalytic measurement set up is shown in figure 2.11(a). A photograph of the experimental photocatalytic measurement set-up is shown in figure 2.11(b).

2.11 Density functional theory and computational technique

The difficulty in the application of Schrodinger's wave equation in many-body problems is overcome using DFT. DFT provides various information about the electronic structure of many-electron systems [25]. All calculations in DFT are based on the assumption that the total ground state energy of a many-electron system is a functional of the electron density. Thus all the ground state properties of a many-electron system can be determined by simply computing the electron density. Unlike the many-body wave function which is a function of 3N variables (the coordinates of all N atoms in the system), the electron density is only a function of three variables i.e three coordinates x, y and z which makes the calculation much easier and faster. The total energy of the system can be expressed as equation 2.14.

$$E_T = E_{ke} + E_{kn} + E_{p(n-e)} + E_{p(n-n)} + E_{p(e-e)} + E_{xc} \quad (2.14)$$

where E_T, E_{ke}, E_{kn}, $E_{p(e\text{-}n)}$, $E_{p(n\text{-}n)}$, $E_{p(e\text{-}e)}$ and E_{xc} represent total ground state energy, the kinetic energy of the electron, the kinetic energy of nucleus, nucleus-electron potential energy, nucleus-nucleus potential energy, electron-electron potential energy and exchange-correlation energy respectively. All the terms in equation 2.14 are functional of electron density. Thus we can write equation 2.15 as

$$E_T = E_T(n) \tag{2.15}$$

where n is the electron density. To obtain the exchange-correlation energy term accurately approximations are to be considered and the most widely used approximation is the local-density approximation (LDA) and generalized gradient approximation (GGA) [26-29].

Application of DFT calculation to study the effect of doping W atom(s) in the MoS_2 system is discussed in detail in chapter 5. The variation of band structure and its type in the compound MoW-disulfide system was studied in this work. Total density of states (TDOS) and Partial density of states (PDOS) of all the three systems was investigated. For this purpose, three clone systems were modeled. In the first model, a system of 8 molecules of MoS_2 was constructed and symbolized as $(MoS_2)_8$. In the second model, the effect of W doping in the first system was studied and one W atom was inserted into it to construct the Mo_8WS_{16} system. To study the impact of W atom the quantity of W atom is made equal to that of Mo atom in the third system $Mo_8W_8S_{16}$. To perform the various calculation GGA with Perdew-Burke-Ernzerhof (PBE) functional was used to describe the electron-electron exchange and correlation effects [29,30]. The DFT equations were solved via projector augmented wave (PAW) method using plane wave basis set as implemented in VASP and interfaced with MedeA technology platform [31].

References

[1] Bernardi, M., Ataca, C. and Grossman, M. J. C. Optical and Electronic Properties of Two-Dimensional Layered Materials *Nanophotonics.*, 5:111-125, 2016. DOI:10.1515/nanoph2015-0030

[2] Jin, W., Yeh, P. C., Zaki, N., Zhang, D., Sadowski, J. T., Al-Mahboob, A., Zande, A. M. V. D., Chenet, D. A., Dadap, J. I., Herman, I. P. Sutter, P., Hone, J. and Osgood R. M. Direct Measurement of the Thickness-Dependent Electronic Band Structure of MoS2 Using Angle-Resolved Photoemission Spectroscopy. Jr. *Phys. Rev. Lett.*, 111:106801, 2013. DOI:10.1103/PhysRevLett.111.106801

[3] Rao, C. N. R. and Nag, A. Inorganic Analogues of Graphene. *Eur. J. Inorg. Chem.*, 4244–4250, 2010. DOI: 10.1002/ejic.201000408.

[4] Matte, H. S. S. R., Gomathi, A., Manna, A. K., Late, D. J., Datta, R., Pati, S. K. and Rao, C. N. R. MoS2 and WS2 Analogues of Graphene. *Angew. Chem.*, 122:4153 - 4156, 2010. DOI: 10.1002/ange.201000009

[5] Deepak, F. L., Mayoral, A. and Yacaman, M. J. Faceted MoS2 nanotubes and nanoflowers. *Materials Chemistry and Physics*, 118:392-397, 2009. DOI:10.1016/j.matchemphys.2009.08.003

[6] Duan, X., Wang, C., Shaw, J. C., Cheng, R., Chen, Yu, Li, H., Wu, X., Tang, Y., Zhang, Q., Pan, A., Jiang, J., Yu, R., Huang, Y. and Duan, X. Lateral epitaxial growth of two-dimensional layered semiconductor heterojunctions. *Nature Nanotechnology*, 9:1024-1030, 2014. DOI: 10.1038/NNANO.2014.222

[7] Tongay, S., Fan, W., Kang, J., Park, J., Koldemir, U., Suh, J., Narang, D. S., Liu, K., Ji, J., Li, J., Sinclair, R. and Wu, J. Tuning Interlayer Coupling in Large-Area Heterostructures with CVD-Grown MoS2 and WS2 Monolayers. *Nano Lett.*, 14:3185-3190, 2014. DOI:10.1021/nl500515q

[8] Pourabbas, B. and Jamshidi, B. Preparation of MoS2 nanoparticles by a modified hydrothermal method and the photo-catalytic activity of MoS2/TiO2 hybrids in photo-oxidation of phenol. *Chemical Engineering Journal*, 138:55-62, 2008.

[9] Zhang, T., Kong, L.-B., Dai, Y.-H., Yan, K., Shi, M., Liu, M.-C., Luo, Y.-C. and Kang, L. A Facile Strategy for the Preparation of MoS3 and its Application as a Negative Electrode for Supercapacitors. *Chem. Asian J.*, 11:2392 – 2398, 2016.

[10] Liang, K. S., Cramer, S. P., Johnston, D. C., Chang, C. H., Jacobson, A. J., Neufville, J. P. d. and Chianelli, R. R. Amorphous MoS_3 and WS_3. *Journal of Non-Crystalline Solids* 42:345-356, 1980.

[11] https://chemiday.com/en/reaction/3-1-0-7653 , accessed on 29.07.2018.

[12] Scott, R. A., Jacobson, A. J., Chianelli, R.R., Pan, W.-H., Stiefel, E. I., Hodgson, K. O. and Cramer, S. P. Reactions of MoS3, WS3, WSe3, and NbSe3 with Lithium. Metal Cluster Rearrangement Revealed by EXAFS. *Inorg. Chem.*, 25:1461-1466, 1986.

[13] Eckert, M. Max von Laue and the discovery of X-ray diffraction in 1912. *Annalen der Physik*. 524(5):A83-A85, 2012. DOI:10.1002/andp.201200724.

[14] Cullity, B. D. and Stock, S. R. *Elements of X-ray Diffraction, Third Edition*. Prentice-Hall, New York, 2001.

[15] Ray F. Egerton. *Physical Principles of Electron Microscopy: An Introduction to TEM, SEM, and AEM*, Springer, Edmonton, Alberta, Canada, 2005.

[16] Gouadec, G. and Colomban, P. Raman Spectroscopy of Nanomaterials: How Spectra Relate to Disorder, Particle Size and Mechanical Properties. *Progress in Crystal Growth and Characterization of Materials*, 53 (1):1-56, 2007.

[17] Chetia, L., Kalita, D. and Ahmed, G. A. Enhanced photocatalytic degradation by diatom templated mixed phase titania nanostructure. *Journal of Photochemistry and Photobiology A: Chemistry*, 338:134-145, 2017. DOI:10.1016/j.jphotochem.2017.01.035

[18] Kalita, D., Chetia, L., Ahmed and G. A. Synthesis of MoW-Sulfide compound nanoparticles as a photocatalyst and comparison of its performance with MoS2 and WS2 nanoparticles. *Journal of Environmental Chemical Engineering*, 5:3161–3171, 2017. DOI: 10.1016/j.jece.2017.06.020

[19] Gfroerer, T. H. Photoluminescence in Analysis of Surfaces and Interfaces, In R.A. Meyers (Ed.), *Encyclopedia of Analytical Chemistry*, pages 9209-9231, John Wiley & Sons Ltd, Chichester, 2000.

[20] Brunauer, S., Emmett, P. H. and Teller, E. Adsorption of Gases in Multimolecular Layers. *J. Am. Chem. Soc.*, 60 (2):309-319, 1938. DOI:10.1021/ja01269a023

[21] https://en.wikipedia.org/wiki/BET_theory , accessed on 09.09.2018.

[22] Kar, R., Gupta, O., Mandol, K. and Bhattacharjee, S. Performance Study on Photocatalysis of Phenol Solution in a UV Irradiated Reactor. *J Chem Eng Process Technol.* 4(1): 143-149, 2013. DOI:10.4172/2157-7048.1000143

[23] Sahoo, C., Gupta, A. K. and Pillai, I. M. S. Heterogeneous photocatalysis of real textile wastewater: Evaluation of reaction kinetics and characterization. *Journal of Environmental Science and Health, Part A*, 47:2109–2119, 2012. DOI: 10.1080/10934529.2012.695996

[24] Mukhlish, M. Z. B., Najnin, F., Rahman, M. M. and Uddin, M. J. Photocatalytic Degradation of Different Dyes Using TiO2 with High Surface Area: A Kinetic Study. *J. Sci. Res.* 5 (2):301-314, 2013. DOI: 10.3329/jsr.v5i1.11641

[25] Harrison, N. M. An introduction to density functional theory. Retrieved on 11.09.2018 from https://www.researchgate.net/publication/30411373_An_introduction_to_density_functional_theory, 2018.

[26] Perdew, J. P. Generalized gradient approximations for exchange and correlation: A look backward and forward. *Physica B*, 172: l-6, 1991.

[27] Perdew, J. P., Chevary, J. A., Vosko, S. H., Jackson, K. A., Pederson, M. R. and Singh, D. J., Fiolhais, C. Atoms, molecules, solids, and surfaces: Applications of the generalized gradient approximation for exchange and correlation. *PHYSICAL REVIEW B*, 46(11):6671-6687, 1992.

[28] Becke, A. D. Completely numerical calculations on diatomic molecules in the local-density approximation. *PHYSICAL REVIEW A*, 33(4):2786-2788, 1986.

[29] Burke, K., Perdew, J. P. and Ernzerhof, M. Why the Generalized Gradient Approximation Works and How to Go Beyond It. *International Journal of Quantum Chemistry*, 61:287-293, 1997.

[30] Ernzerhof, M. and Scuseria, G. E. Assessment of the Perdew-Burke-Ernzerhof exchange-correlation functional. *J. Chem. Phys.*, 110:5029-5036,1999. DOI:10.1063/1.478401

[31] Kresse, G., Marsman, M. and Furthmüller, J. VASP the GUIDE. Retrieved on 27.02.2015 from http://wolf.ifj.edu.pl/workshop/work2008/tutorial/vasp.pdf , 2005.